

A 1.3-micrometre-thick elastic conductor for seamless on-skin and implantable sensors

Received: 16 March 2022

Accepted: 12 October 2022

Published online: 21 November 2022

 Check for updates

Zhi Jiang^{1,2}, Nuan Chen², Zhigao Yi³, Junwen Zhong^{4,8}, Feilong Zhang², Shaobo Ji², Rui Liao⁵, Yan Wang⁶, Haicheng Li², Zhihua Liu⁷, Yang Wang⁵, Tomoyuki Yokota⁶, Xiaogang Liu³, Kenjiro Fukuda^{1,8}, Xiaodong Chen^{2,7} & Takao Someya^{1,6,8}

On-skin and implantable electronics require elastic conductors that are only a few micrometres thick and soft enough to form a seamless contact with three-dimensional structures. However, fabricating thin conductors that are mechanically durable and have consistent electrical properties with stretching is challenging. Here we report polydimethylsiloxane (PDMS)–gold conductors that are around 1.3 μm thick and have a controlled morphology of microcracks in the gold film. The microcracks are formed by evaporating a 50-nm-thick gold film onto a 1.2- μm -thick PDMS film that is supported during fabrication by a 100- μm -thick PDMS film on glass; thermal expansion of the thick PDMS film causes the evaporated gold to form a microcracked structure on the thin PDMS. The resulting conductors can be stretched by up to 300% and remain highly conductive after strain release. We use them to create on-skin electrodes that are breathable and water resistant, and can continuously record electrocardiogram signals. We also use the conductors to create on-skin sensors with less than 3 μm thickness that can detect small mechanical forces and create implantable nerve electrodes that can provide signal recording and stimulation.

Stretchable conductors that are thin and highly conformable are essential for the development of on-skin and implantable electronics^{1–5}. Such conductors are fabricated on soft and thin substrates, and should exhibit a high, stable conductivity after repeated deformations. They should also offer a thinness and softness that allows them to form a seamless contact with undevelopable surfaces, as well as compatibility and adhesion to skin and organs^{6–8}. The conductors are typically made from a blend of stretchable polymers (such as polydimethylsiloxane (PDMS), styrene–ethylene–butylene–styrene, polyurethane or fluorine rubber^{9–12}) and conductive fillers (such as nanowires, nanoparticles,

carbon nanotubes or graphene^{11–15}). In particular, by using metallic nanowires with high aspect ratios as the conductive filler¹⁶, and aligning them on a thin polymer layer, high conductivity and stretchability can be simultaneously achieved¹⁷. Alternatively, large deformations are possible with liquid-metal-based conductors due to their intrinsic fluidic property^{18,19}.

The thickness and softness of both substrate and conductor are important in the development of conformable electronics, and these components should also be compatible with the manufacturing processes of electronic/optical devices with multistacked

¹Thin-Film Device Laboratory, RIKEN, Wako, Saitama, Japan. ²Innovative Center for Flexible Devices (iFLEX), School of Materials Science and Engineering, Nanyang Technological University, Singapore, Singapore. ³Department of Chemistry, National University of Singapore, Singapore, Singapore. ⁴Department of Electromechanical Engineering and Centre for Artificial Intelligence and Robotics, University of Macau, Macau, People's Republic of China. ⁵State Key Laboratory of Electronic Thin Films and Integrated Devices, School of Optoelectronic Science and Engineering, University of Electronic Science and Technology of China (UESTC), Chengdu, People's Republic of China. ⁶Department of Electrical Engineering and Information Systems, The University of Tokyo, Tokyo, Japan. ⁷Institute of Materials Research and Engineering, Agency for Science, Technology and Research (A*STAR), Singapore, Singapore. ⁸Center for Emergent Matter Science, RIKEN, Wako, Saitama, Japan. ✉e-mail: kenjiro.fukuda@riken.jp; chenxd@ntu.edu.sg; takao.someya@riken.jp

structures. Recently, polyurethane–PDMS nanofilms with thicknesses of around 90 nm have been created that exhibit good adhesion to the skin and good gas permeability²⁰. However, the nanofilms have a vapour-deposited 70-nm-thick gold (Au) layer that offers a maximum stretchability of around 30% with stable conductivity due to the coarse surface of the nanofilms. For on-skin and implantable applications, thin elastic conductors need to offer a stretchability of 100% or more and maintain stable conductivity, to prevent damage during the handling process.

One promising approach to address this is to create metallic microcracks on thin elastic substrates²¹. The microcracked surface prevents further damage to occur under stretch. Studies on microcrack-based conductors have focused on the combination of Au and PDMS, and 10- μm -thick PDMS–Au conductors have been created that have a maximum stretchability of around 80% (refs. ^{9,22}). However, the conductivity of these conductors dramatically decreased on deformation. The formation of Au microcracks requires thermal expansion of the PDMS substrates during thermal evaporation. However, thin PDMS substrates are insufficiently deformed during evaporation, which can lead to Au films with low stretchability and without microcracked structures.

In this Article, we report gas-permeable ultrathin elastic conductors that are made from Au microcracks on thin PDMS substrates. The electrodes have a total thickness of around 1.3 μm , and consist of a 50-nm-thick Au layer and 1.2- μm -thick PDMS film (Fig. 1a,b). During fabrication, the ultrathin PDMS is supported by a 100- μm -thick PDMS film on glass. Thermal expansion of the thick PDMS film causes the evaporated Au to form a microcracked structure on the ultrathin PDMS. The resulting electrode exhibits a fracture strain of around 350% (Fig. 1d) and can hold a weight of 20 g and remain conductive (Fig. 1c and Supplementary Figs. 1 and 2). Due to their ultrathin thicknesses and soft mechanical properties, the electrodes can form seamless contacts with human skin and a rat nerve (Fig. 1e,f). When combined with a thin ionic conductive polymer layer, the electrodes show strong adhesion to skin even in water, and we illustrate their potential to monitor biosignals in daily life and during exercise by using it to continuously record electrocardiography (ECG) signals. We also create on-skin pressure sensors for detecting small mechanical forces such as the arterial pulse wave and create implantable nerve electrodes for neuromodulation and signal recording.

Design principle and mechanism

To obtain the microcrack morphology of the Au layer of the micrometre-thick PDMS–Au electrode (Fig. 2), we use a clean 100- μm -thick PDMS layer between the glass substrate and micrometre-thick PDMS during thermal evaporation (Fig. 2a, Supplementary Figs. 3 and 4 and Supplementary Video 1). Microcracks with a tri-branched shape were uniformly distributed in the Au layer, which is critical for good stretchability (Fig. 2b). In contrast, the direct formation of the Au layer on the micrometre-thick PDMS-coated glass without the thick PDMS film showed almost no visible microcracks (only tiny wrinkles, Fig. 2c,d). Without the thick PDMS layer, the ultrathin PDMS–Au (with almost no initial microcracks) lost its conductivity within 17% tensile strain, because long, parallel cracks formed during stretching perpendicular to the stretch direction without any connection between these Au fragments (Fig. 2j and Supplementary Fig. 5). When using the thick PDMS layer during evaporation, the electrode showed a maximum stretchability of around 300% and maintained its conductivity (Fig. 2j and Supplementary Video 2), because shorter, non-parallel cracks form uniformly in the Au layer that are seeded by the initial microcracks that form during the fabrication process, whereas a conductive pathway remains between Au microfragments (Fig. 2b and Supplementary Fig. 5). The resistivity at 0% tensile strain increased from 6.33×10^{-7} to 4.46×10^{-6} and 8.70×10^{-6} Ωm when stretched under 100% and 200% strain, respectively.

The initial microcracked morphology can be used to control the stretchability of PDMS–Au conductors with well-developed theories^{9,21}. However, although it is hypothesized that crack formation is due to the mismatch of the thermal coefficient between PDMS and Au (ref. ⁹), how this microcracked morphology is actually formed has not been fully explained yet. To investigate the formation mechanism, we first fabricated PDMS of different thicknesses on a glass substrate without using the thick PDMS and keeping the other fabrication conditions the same. We found that the density of microcracks on the Au layer dramatically decreased when we reduced the PDMS thickness from 100 to 10 to 1 μm (Supplementary Fig. 6). As a result, the maximum stretchability and conductivity gradually decreased at the same strains (Supplementary Fig. 7). Next, we compared the morphology of thin Au layers of different thicknesses on different PDMS films. We found that on the micrometre-thick PDMS, there were short microcracks with very small gaps when the Au layer was 10 and 20 nm thick, which disappeared when the thickness was increased to 50 and 80 nm (Supplementary Fig. 8). By comparison, there was a microcracked morphology on thick PDMS for 10-, 50- and 80-nm-thick Au layers (Supplementary Fig. 9).

To explain how the PDMS thickness could influence the morphology of microcracks in the Au layer, we conducted finite element analysis (FEA) using the COMSOL software. The microcrack geometry was simplified into regular shapes (namely, Y, T, I and X) to simulate the arrays of cracks. We found that the entire Au layer (10 nm) on the thick PDMS experienced both in-plane and out-of-plane deformation (Fig. 2e,f), resulting in a larger crack area (Fig. 2e). In contrast, the Au layer on the 1- μm -thick PDMS experienced less deformation at the same temperature, whereas the crack area shrank (Fig. 2g,h). The above phenomenon occurred in a temperature range from 30 to 80 °C, which is estimated to be comparable to that of thermal evaporation (Fig. 2i and Supplementary Figs. 10 and 11)²³. Considering that the thermal deformation of Au microcracks and the deposition of Au simultaneously occurred during thermal evaporation, the crack area—if not increasing—would gradually disappear with Au deposition, consistent with our experimental results (Fig. 2d). From the above results, it can be concluded that the microcracked morphology was formed in the initial stages of thermal evaporation and that the thickness of PDMS had a notable influence on the preservation of microcracked morphology by influencing the crack growth (Supplementary Fig. 12). Additionally, we found that thermal stress was critical for the formation of microcracked morphology⁹. We post-annealed the samples with few Au microcracks on the 1- μm -thick PDMS-coated glass. The 20-nm-thick Au film showed little change after post-annealing at 100 °C for 5 min, whereas the same film showed dramatically increased microcracks after post-annealing at 200 °C for 5 min (Supplementary Fig. 13). By contrast, the 80-nm-thick Au film showed no microcracks even after post-annealing at 200 °C for 5 min (Supplementary Fig. 14). The above results indicate that a high temperature can contribute to crack formation due to the large thermal stress, but it may degrade the mechanical properties of the PDMS film itself if the temperature is too high^{24,25}.

We next characterized the change in morphology and mechanical stability of the ultrathin PDMS–Au electrodes. During deformation, microcracks propagated and smaller Au fragments formed (Supplementary Fig. 15). Because these Au microfragments were still in physical contact with each other, the conductive pathways were maintained. In addition, owing to the good recovery ability of PDMS, the microcracked morphology was reversible on strain release. As a result, the electrodes showed good stability at 0% strain with little differences when changing the deformation speed from 0.5 to 6.0 mm s^{-1} at a maximum tensile strain of 100% (Fig. 2k,l). Moreover, the electrodes were stable at 0% strain during 5,000 cycles of the stretch/release test at a maximum tensile strain of 100% (Fig. 2m)—a durability that was among the best stretchable conductors at 0% strain (Supplementary Fig. 16 and Supplementary Table 1). These properties are very important for their practical applications in ultrathin elastic electronic devices.

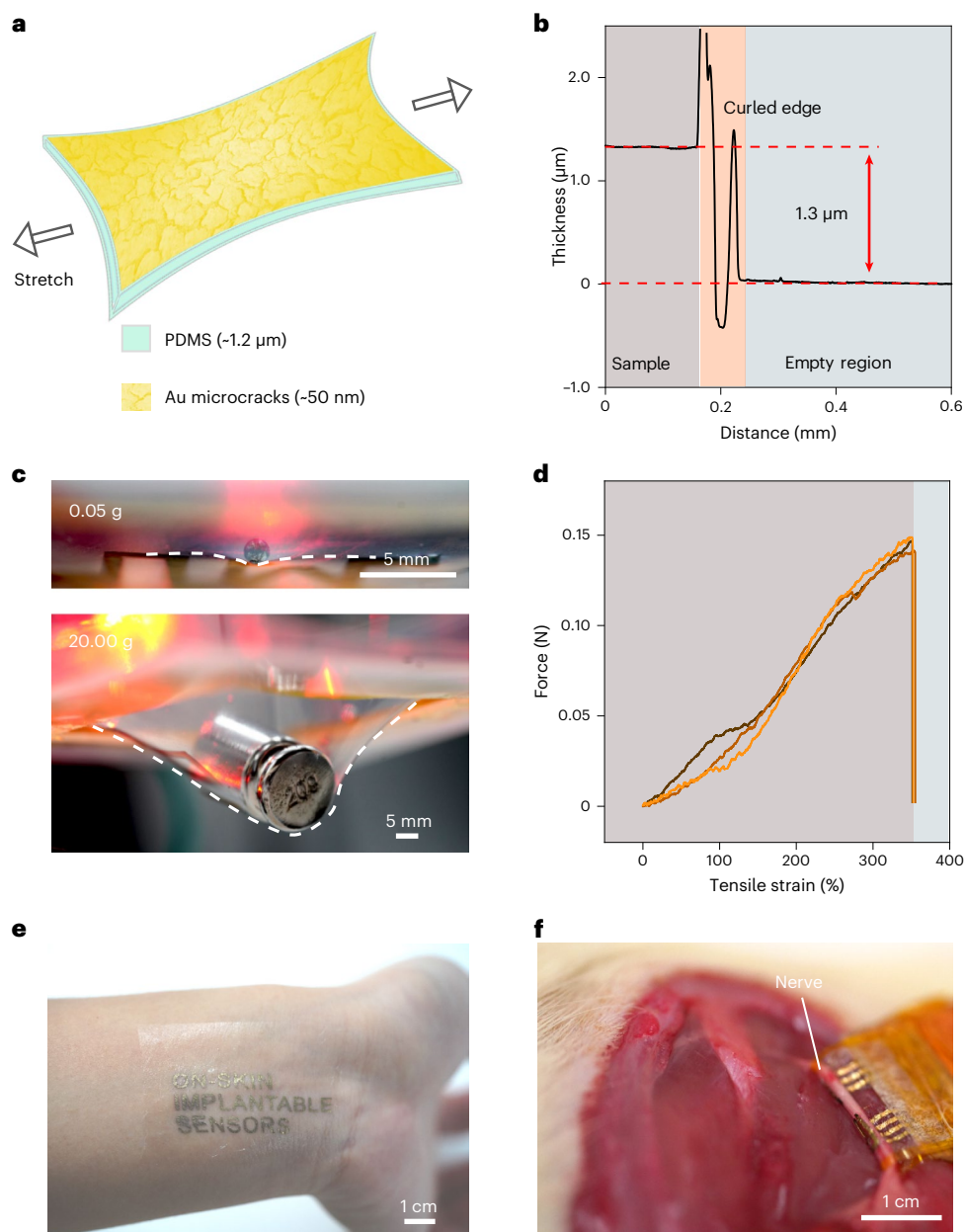


Fig. 1 | Design of stretchable ultrathin conductors. **a**, Structural illustration of the PDMS–Au conductor, where PDMS has a thickness of $\sim 1.2\ \mu\text{m}$ and the Au layer with microcracked morphology has a thickness of $\sim 50\ \text{nm}$. **b**, Surface profile of the conductor, showing a thickness of approximately $1.3\ \mu\text{m}$. **c**, Optical images (front view) of the freestanding conductor deformed by objects of different

weights. The conductor remains conductive under the above deformation, as shown by the red LED light. **d**, Curve of tensile force versus tensile strain of the conductor with a width of $6.0\ \text{mm}$ and length of $3.5\ \text{mm}$. **e, f**, Optical images of the ultrathin PDMS–Au electrodes attached onto human skin (**e**) and a rat nerve (**f**), exhibiting a seamless contact.

Another important parameter for the application of electrodes in ultrathin elastic electronic devices is its patterning ability. The linewidth could be downscaled to $40\ \mu\text{m}$, and the fine lines showed good cyclic durability (Supplementary Fig. 17). In addition, we examined the applicability of the facile strategy (Fig. 2a) for other conductive materials. We found that the conductive layer should be ductile, such as Au and Ag (Supplementary Fig. 18), and not brittle, such as indium tin oxide (Supplementary Fig. 19), to form a connected microcracked morphology.

Reducing the thickness of elastic conductors from 100 to $1\ \mu\text{m}$ has three main benefits. (1) Improved gas permeability: a bottle covered with the ultrathin PDMS–Au electrodes showed a water loss speed of $11.9\ \text{mg h}^{-1}\ \text{mm}^{-2}$, which was much higher than that of $100\text{-}\mu\text{m}$ -thick

PDMS–Au ($3.5\ \text{mg h}^{-1}\ \text{mm}^{-2}$) (Supplementary Fig. 20) and the trans-epidermal water loss speed of human skin ($4.0\text{--}10.0\ \text{mg h}^{-1}\ \text{mm}^{-2}$) (ref. ²⁶). (2) Minimized mechanical stress: theoretically, reducing the thickness of the conductor from 100 to $1\ \mu\text{m}$ reduces the tensile force exerted on other objects when it deforms by a factor of 100 . For the ultrathin PDMS–Au electrodes with a width of $6.0\ \text{mm}$, a small force of $38.9\ \text{mN}$ was needed to achieve 100% deformation (Fig. 1c), which is much smaller than the force ($\sim 1\ \text{N}$) of the continuous stratum corneum of human skin with a thickness of $\sim 20\ \mu\text{m}$ and width of $5\ \text{mm}$ at 1% deformation²⁷. (3) Improved conformability: the ultrathin design led to dramatically reduced stiffness with excellent conformability, improving contact between the device and curved surfaces²⁸. The above three properties are important for biocompatible on-skin and

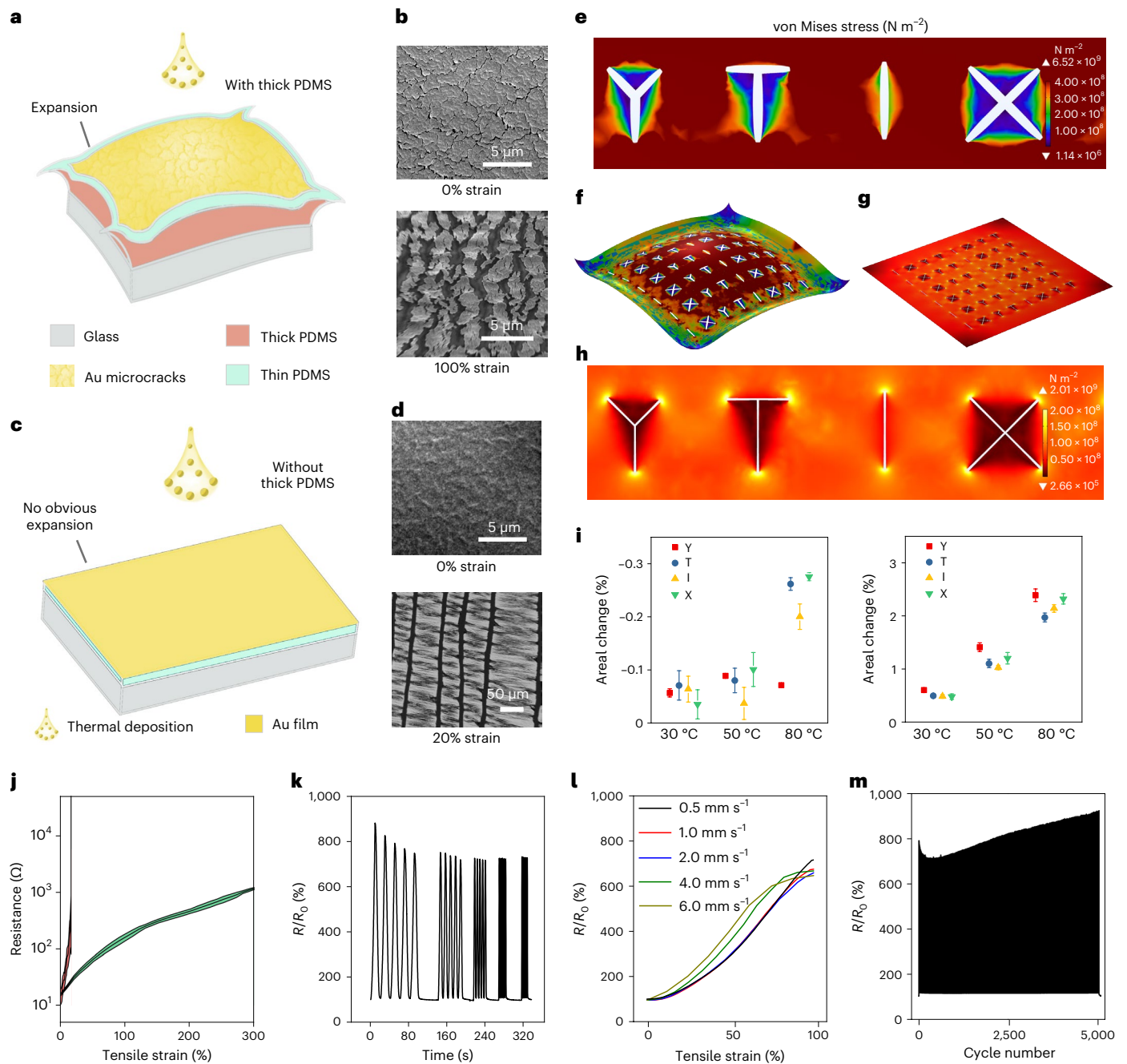


Fig. 2 | Mechanism of microcracked morphology formation and mechanical/electrical characterization. **a**, Structural illustration of the crack formation on ultrathin PDMS–Au conductors during thermal evaporation. **b**, Scanning electron microscopy (SEM) images of the conductor (after peeling off from the supporting substrate) under 0% (left) and 100% (right) tensile strain. The SEM observation was repeated three times. **c**, Structural illustration of 1- μm -thick PDMS–Au without applying the key approach. **d**, SEM image of 1- μm -thick PDMS–Au without applying the key approach at 0% strain (left) and optical image at 20% strain (right). The SEM observation was repeated three times. **e–h**, Comparison of the simulated strain distribution and deformation of the Au layer on the PDMS substrate of different thicknesses at a steady temperature of 80 °C: 100- μm -thick

PDMS (**e** and **f**) and 1- μm -thick PDMS (**g** and **h**). Note that the surface deformation is amplified by a factor of 10 in both cases ($n = 12$ for all conditions). **i**, Statistical data of the crack area change for both simulated models at different temperatures ($n = 4$ for all conditions). Data are presented as mean \pm standard error of the mean (s.e.m.). **j**, Comparison of the conductivity under different tensile strains between the ultrathin conductor and 1- μm -thick PDMS–Au without using the key approach. **k**, Stability of the conductor against a series of deformation speeds at 100% tensile strain—the speeds being 0.5, 1.0, 2.0, 4.0 and 6.0 mm s^{-1} (from left to right). **l**, Comparison of the change in resistance (R/R_0) of the ultrathin conductor at different strains under different stretch speeds. **m**, Stability of the conductor during 5,000 cycles of the stretch/release process at 100% tensile strain.

implantable bioelectronics^{1,16,29}. Reducing the total thickness of the device to below 1 μm could lead to additional functionalities including robust self-adhesion and lower or no immune response^{20,30}. There are, however, technical challenges involved in handling such films. For example, a PDMS film with a thickness of around 500 nm cannot

be completely peeled off from the thick PDMS support layer on glass because of strong adhesion and low fracture point. Furthermore, the target application should determine the most suitable thickness of the stretchable conductor. For on-skin sensing electrodes, a thinner device is desirable as this leads to more stable contact and lower mechanical

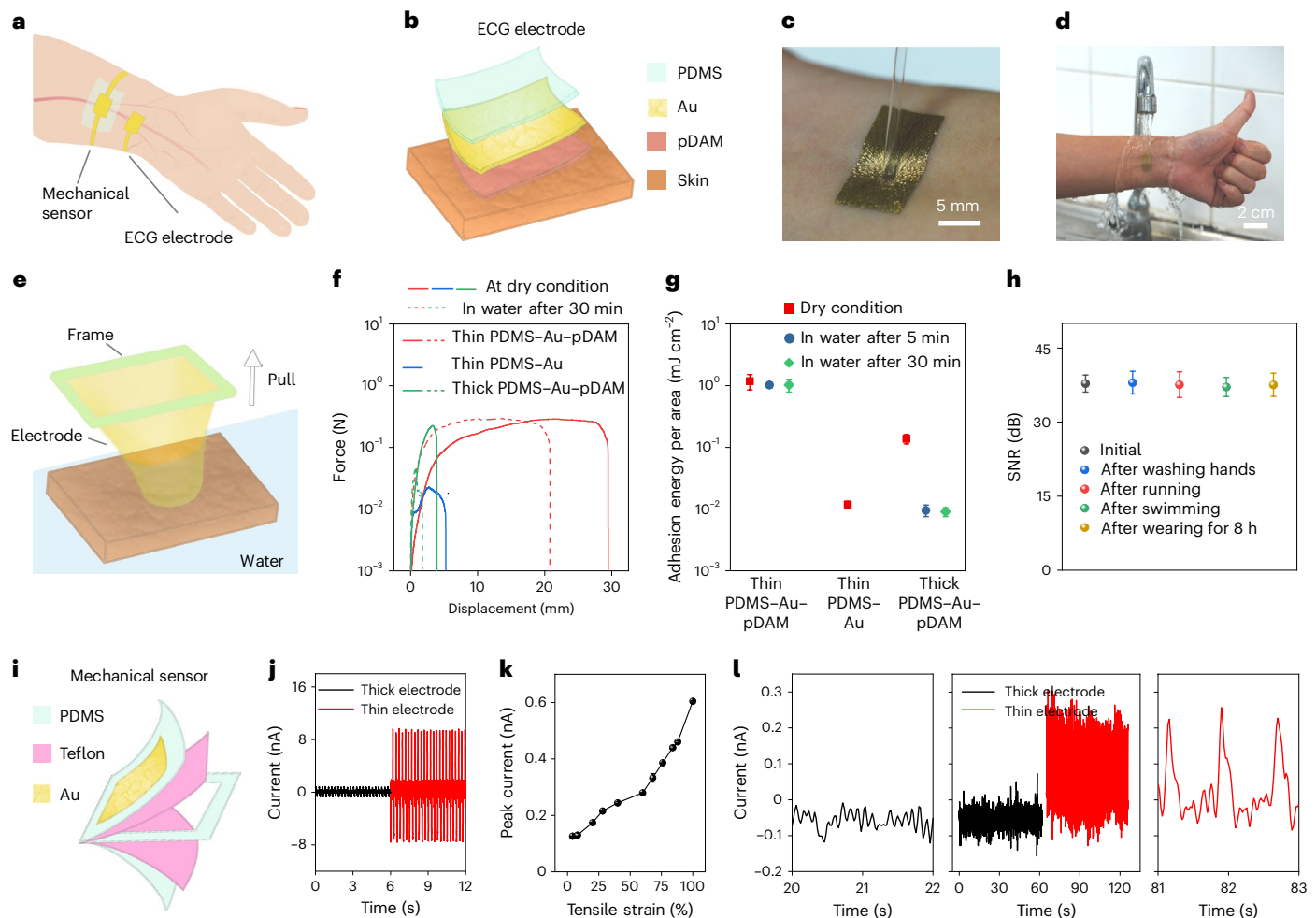


Fig. 3 | On-skin sensors based on ultrathin conductors. **a**, Illustration of on-skin signal recording using the ECG electrode and mechanical sensor. **b–h**, Utilization of the ultrathin PDMS–Au–pDAM as the ECG sensor electrodes. Structural illustration (**b**) and optical images of the electrodes on human skin (**c**) and when washed with water (**d**). Structural illustration of the adhesion measurement between the electrodes and skin (**e**). Comparison of displacement versus force curves of different electrodes in dry condition and in water after 30 min (**f**), including the ultrathin PDMS–Au–pDAM, ultrathin PDMS–Au and thick electrode–pDAM. Comparison of the adhesion energy between the above electrodes and skin (**g**). Data are presented as mean \pm s.e.m. Comparison of

the SNR values of the recorded ECG signals under different conditions of the volunteer, including after hand washing, running, swimming and prolonged wearing (**h**). Data are presented as mean \pm s.e.m. **i–l**, Utilization of the ultrathin PDMS–Au electrodes in ultrathin force sensors. **i**, Structure of the sensor. **j**, Comparison of the output signals of the force sensors under a peak pressure of ~ 4.7 kPa between sensors—with the ultrathin PDMS–Au and with thick electrodes. **k**, Peak output current of the sensors under a series of tensile strains. **l**, Comparison of the real-time measurement of carotid arterial pulse wave using the ultrathin sensors and thick sensors.

constraints²⁰. For implantable and cell electronics in wet environments, encapsulation needs to be considered. Since the barrier degrades with decreasing thickness, a thinner device does not guarantee better electrical signals over a long period of time. In addition, modifying the ultrathin PDMS film by adding ultrathin inorganic layers could provide a better barrier against biofluids^{31,32}.

On-skin electrodes and sensors

To demonstrate the potential application of the ultrathin PDMS–Au electrodes for on-skin electronics, we utilized them as on-skin sensing electrodes and as electrodes for micrometre-thick sensors to measure biosignals (Fig. 3a). As dry sensing electrodes, they must adhere to the skin even under wet conditions, and they must also be mechanically robust and gas permeable. To fulfil the above requirements, we formed a 22-nm-thick, ionically conductive polymer layer, such as p(DM-co-AA-co-MEA) (pDAM) (ref. 33), on Au (Fig. 3b). The combination of electrodes and adhesive polymer made it easy to be attached to the skin by forming a seamless contact that was resistant to skin

deformation (Fig. 3c) and strong water rinsing (Fig. 3d). Moreover, the thin pDAM layer did not influence the gas permeability of the electrodes, which is suitable for long-term wear without causing skin problems (Supplementary Figs. 21 and 22)^{19,29}.

Next, we characterized the adhesion property between the electrodes and skin by the peel test (Fig. 3e). The adhesion energy per area (E) was selected as the standard quantification calculated by the integrated area of the displacement versus force curve (Fig. 3f,g and Supplementary Fig. 23). We found that the ultrathin PDMS–Au–pDAM showed the highest E values in the dry state (1.18 ± 0.33 mJ cm⁻²) and in water after 5 min (1.03 ± 0.12 mJ cm⁻²) and 30 min (1.03 ± 0.24 mJ cm⁻²). In comparison, the ultrathin PDMS–Au showed a much lower E value (0.01 ± 0.001 mJ cm⁻²) and lost adhesion with the skin in water (Supplementary Fig. 24). For the thick electrode with pDAM, the E values decreased from 0.14 to 0.01 mJ cm⁻² because the contact with the skin was not seamless, and pDAM was too thin. As a result, when washing hands with water, only the ultrathin PDMS–Au–pDAM was stable on the skin, whereas the ultrathin PDMS–Au shrank (Supplementary Video 3),

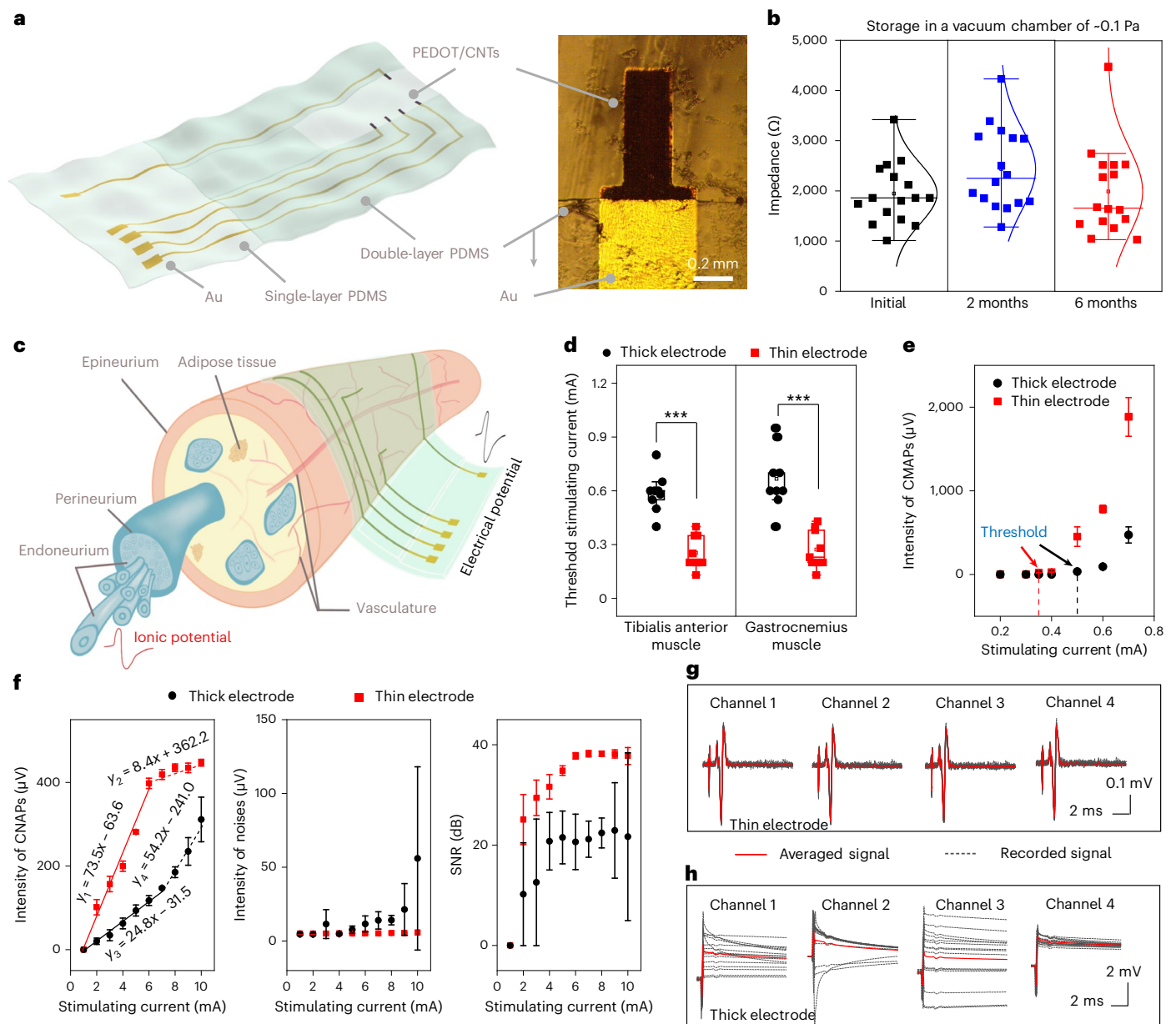


Fig. 4 | Implantable neural interfaces based on ultrathin conductors. a, Structure of the electrodes (left) and the optical image of the electrode site (right). **b**, Impedance of the electrodes at a frequency of 1 kHz before and after storage for six months in a vacuum chamber of -0.1 Pa ($n = 4$ for all the conditions). **c**, Illustration of the electrode attached to a nerve, forming a seamless contact between them. **d, e**, Utilization of neural electrodes for nerve stimulation. Comparison of the threshold current for the ultrathin electrodes and thick electrodes to activate muscles during nerve stimulation ($n = 3$ for both electrodes) (**d**). From bottom to top, the box plots include the minimum current, first (lower) quartile, median, third (upper) quartile and maximum current. Statistical significance is indicated using *** for $p < 0.001$ (a one-way analysis of

variance test was carried out with Tukey's multiple comparisons test). Data are presented as mean \pm s.e.m. Representative comparison of CMAPs on muscles by changing the stimulation current on nerves via the ultrathin electrodes and thick electrodes ($n = 3$ for both electrodes) (**e**). **f–h**, Utilization of neural electrodes for signal recording. Comparison of the intensity of CNAPs, noise and SNR values of CNAPs recorded with the ultrathin electrodes and thick electrodes ($n = 3$ for both electrodes) (**f**). Data are presented as mean \pm s.e.m. CNAPs recorded from the four channels of the ultrathin electrodes under a stimulating current of 10 mA at the paw (**g**). CNAPs recorded by the four channels of thick electrodes under a stimulation current of 10 mA at the paw (**h**).

and thick electrode–pDAM was washed away (Supplementary Video 4). Combined with the skin mimic structure, ultrathin PDMS–Au showed stable resistance under fierce arm movement (Supplementary Video 5 and Fig. 25). Finally, only the ultrathin PDMS–Au–pDAM electrodes were able to continuously record ECG signals after the volunteer conducted strenuous exercise such as running and swimming and after washing hands and wearing the electrodes for 8 h (Supplementary Figs. 26 and 27). The signal-to-noise ratio (SNR) values were stable at

37.5 dB after the above activities (Fig. 3h), ensuring the continuous monitoring of biosignals in daily life without disturbance. Moreover, the ultrathin pDAM layer worked well for 1- μ m-thick polyurethane nanofibre–PDMS–Au, indicating its universal applicability (Supplementary Fig. 28).

In addition to single-layer on-skin sensing electrodes, the ultrathin PDMS–Au electrodes can be utilized in an electronic device with multiple layers, that is, a mechanical sensor (Supplementary Fig. 29, less

than 3 μm), which was much thinner than previously reported similar sensors (thickness, 89 μm)³⁴. The ultrathin sensor was constructed by separating two thin Teflon AF films by an air gap and sandwiched them between two electrodes consisting of our ultrathin PDMS–Au electrodes (Fig. 3i). The sensors showed piezoelectric-like performance with sensitivity to both compressive and extensional stresses (Supplementary Fig. 30 and Supplementary Video 6). The ultrathin sensors showed notably higher compressive sensitivity than the thick sensors (Fig. 3j and Supplementary Figs. 31–33). The ultrathin sensors exhibited increased peak output current with increasing tensile strain—from 0% to 100% (Fig. 3k and Supplementary Fig. 34)—and good cyclic resistance to both compression and tensile strain tests up to 43,200 cycles (Supplementary Figs. 35 and 36). Finally, the ultrathin sensors successfully measured the arterial pulse wave (Fig. 3l), whereas the thick sensors failed under the same conditions due to lower sensitivity. Compared with piezoresistive and capacitive sensors, our ultrathin sensors do not need an external power supply on the sensor itself and showed stable performance after thousands of cyclic tests³⁵. Compared with single-layer thin triboelectric and hybrid piezo-/triboelectric sensors, our ultrathin sensors exhibit good piezoelectric property and encapsulation, which contribute to a high signal output and good environmental stability (Supplementary Fig. 37 and Supplementary Video 6)^{36,37}. Since ultrathin sensors are soft, sensitive and durable, they hold great promise for biocompatible wearable electronics and soft robotics applications^{38,39}.

Implantable neural electrodes

To demonstrate the application potential of ultrathin PDMS–Au electrodes for implantable electronics, we developed cuff-type micrometre-thick neural electrodes as high-quality interfaces for modulation/signal recording with nerves. The electrodes coated with poly(3,4-ethylenedioxythiophene) (PEDOT)/carbon nanotubes (CNTs) (Fig. 4a and Supplementary Figs. 38 and 39)⁴⁰ showed a low impedance (1.95 k Ω at 1 kHz in saline) and remained stable after storage for six months in a vacuum chamber (0.1 Pa) and after immersing in saline at room temperature for 973 h (Fig. 4b and Supplementary Figs. 40 and 41). Owing to their extreme deformability, a seamless interface formed between the ultrathin electrodes and nerve tissues without the use of adhesive or sutures, which should result in less damage to nerves compared with previous reports (Figs. 1f and 4c, Supplementary Fig. 42 and Table 2)⁴¹. In contrast, there was an obvious gap at the interface between the thick electrodes and nerve tissue (Supplementary Figs. 42 and 43). The seamless interface between the ultrathin electrodes and tissue participates in effective stimulation delivery and signal recording, especially for ultras-small (-microvolts) and noise-ridden neural signals.

To evaluate the neuromodulation ability, we electrically stimulated the sciatic nerve through the developed electrodes and recorded compound muscle action potentials (CMAPs) from the gastrocnemius and tibialis anterior muscles (Supplementary Fig. 44). A common phenomenon for both ultrathin electrodes and thick electrodes was that selective muscle activation was successfully achieved by stimulating different fascicles underneath the electrode pairs (Supplementary Videos 7 and 8). However, to elicit muscle activation, the average threshold stimulation current (0.32 mA) of the ultrathin electrodes was significantly lower than that for thick electrodes (0.56 mA), and the CMAP values were much higher at the same stimulation current (Fig. 4d,e and Supplementary Fig. 45). Next, we exploited the electrodes to record compound nerve action potentials (CNAPs) evoked by the subdermal electrical stimulation of the rat paw. Both electrodes recorded CNAPs with higher intensity when the stimulation current was increased, but the values for the ultrathin electrodes were significantly higher (~2–4 times) at the same stimulation (Fig. 4f). Owing to the stable and seamless contact (Fig. 1f), the noise level for the ultrathin electrodes remained stable when the stimulation current was increased. In sharp contrast, the noise dramatically increased for the 100- μm -thick

electrodes due to movement artifacts (Fig. 4f). For example, the baseline of CNAPs recorded from the thick electrodes dramatically shifted when the stimulation current was 10 mA, making it difficult to distinguish CNAPs (Fig. 4h). In contrast, all the channels of the ultrathin electrodes successfully recorded high-quality CNAPs under the same current (Fig. 4g). As a result, the SNR values for the ultrathin electrodes were significantly higher than those for the thick electrodes, especially when the stimulation was strong (Fig. 4f). These combined results demonstrate that the ultrathin design greatly improved neuromodulation and signal recording through a seamless contact. Considering that the ultrathin electrodes utilized fully biocompatible materials^{40,42} and demonstrated the ability to provide high-quality recording and neuromodulation with selectivity, they hold promising applications in implantable electronics, such as peripheral nerve electrodes for closed-loop neuroprosthetics and implantable sensing electrodes for in vivo ECG signal recording^{41,43}.

One limitation for the current ultrathin electrode is the increased resistance under stretching, which is similar to other stretchable conductors using solid metal films or composites^{9–17}. However, our demonstrated applications do not need to work under large strains. If there is a need that the device should maintain the same performance under large strains, the resistance change in the conductors under such strains should be minimized using other materials, such as liquid metals^{18,19}.

Conclusions

We have reported a 1.3- μm -thick stretchable PDMS–Au conductor with a maximum stretchability of 300.0% and good mechanical durability (1.7% resistance increase at 0% strain after 5,000 cycles at 100.0% strain). We used our ultrathin conductors to create on-skin electrodes that are breathable, water resistant and can be used to continuously record ECG signals during daily life as well as during strenuous exercise such as running and swimming. We also use the conductors to create 3- μm -thick stretchable sensors that can detect small mechanical forces, and to create implantable sensing and stimulation electrodes. The cuff-type ultrathin neural electrodes could deliver electrical stimulations more effectively to a sciatic nerve (2–4 times higher than that for thicker electrodes) and record stable neural signals with much lower noises compared with thicker electrodes.

Methods

Materials

PDMS GYL GARD 184 was purchased from Dow Corning; Teflon AF 1600, from DuPont; and hexane, from Wako Chemicals. All these materials were directly used without any further treatment.

Fabrication of ultrathin PDMS–Au conductor

First, we prepared the PDMS solution by mixing the base and crosslinking agent at a weight ratio of 10:1 and removed bubbles by vacuuming. Then, we prepared the polyimide frame, directly cut from a commercial polyimide film (3M) of thickness 125 μm using a green laser (KEYENCE MD-T1010W). It should be noted that a polyimide frame (or 3M double-sided tape with a paper cover) is necessary for the fabrication and handling process of the micrometre-thick PDMS film, as freestanding ultrathin soft PDMS film can easily curl without any supporting substrate or frame. Unless the ultrathin film is transferred onto the human skin or a rat nerve or the mechanical testing machine, the frame must not be removed. To adhere the polyimide frame onto the glass, it was immersed in the diluted PDMS solution (1 wt% in hexane) before the attachment. The glass substrate was modified using a releasing layer, that is, Teflon AF 1600 (DuPont). The Teflon AF 1600 layer was necessary because it could reduce the adhesion between the thin PDMS and glass substrate. To solidify the thin PDMS layer, the sample was heated at 110 $^{\circ}\text{C}$ for 10 min.

Next, we spin coated the diluted PDMS solution (25 wt% in hexane) or undiluted PDMS solution on the glass substrate at different speeds to control the thickness. For the standard recipe, we spin coated the

diluted PDMS solution (25 wt% in hexane) on a glass substrate at a speed of 6,000 rpm for 60 s to obtain an ultrathin PDMS substrate with a thickness of ~ 1.2 μm . Meanwhile, we spin coated undiluted PDMS on the glass substrate at a speed of 1,000 rpm for 30 s to obtain a thick PDMS film with a thickness of ~ 100 μm . We then heated the sample at 110 $^{\circ}\text{C}$ to solidify the PDMS layer with different thicknesses (1.5 min for ultrathin PDMS and 3 min for the thicker PDMS). After solidification, we transferred the micrometre-thick PDMS layer onto the 100- μm -thick PDMS-coated glass substrate (Supplementary Video 1). To form a seamless interface between the ultrathin PDMS and thick PDMS, the surface of the thick PDMS was maintained without dust (Supplementary Fig. 5). Finally, Cr/Au layers (5/50 nm) were deposited on the PDMS layer by thermal evaporation at a speed of 0.02/0.20 nm s^{-1} . After this, we peeled off the ultrathin PDMS–Au conductor from the glass substrate. It should be noted that although the peeling process deformed the ultrathin PDMS–Au conductor, the resistance of the ultrathin PDMS–Au conductor only showed a 0.5% increase in resistance because of the excellent recovery capability of the ultrathin PDMS–Au conductor at 0% strain.

Fabrication of micrometre-thick ECG electrodes

When we conducted the thermal evaporation process to make the ultrathin PDMS–Au conductor, we used a shadow mask to form patterned electrodes. Then, we treated the surface with a weak oxygen plasma treatment (30 W, 12 s). Next, we spin coated the pDAM solution on the sample to modify its surface. The pDAM was synthesized by us according to previous reports¹, and it was dissolved in acetone at room temperature with a concentration of 20 mg ml^{-1} .

Fabrication of micrometre-thick stretchable self-powered sensor

When we conducted the thermal evaporation process to make the ultrathin PDMS–Au conductor, we used a shadow mask to form patterned electrodes. After the evaporation process, we peeled off the ultrathin PDMS–Au conductor and attached it to the Teflon AF 1600-modified glass substrate with the Au layer facing the glass substrate. Next, we treated the PDMS surface using an oxygen plasma treatment at a power of 300 W for 10 s, and formed a Teflon AF 1600 layer by spin coating the Teflon AF 1600 solution (1 wt% in FC-43 solution) at 2,000 rpm for 60 s. We then heated the sample at 100 $^{\circ}\text{C}$ for 30 min to completely remove the solvent. Next, we treated the Teflon layer using an oxygen plasma treatment at a power of 300 W for 1 min and brushed a diluted PDMS solution (1 wt% in hexane) onto the edges of the sample with a thickness of ~ 200 nm after solidification. It should be noted that the plasma treatment on the Teflon surface has two functions: (1) it can promote a tight interface with PDMS after crosslinking PDMS; (2) it acts as the charging process on the Teflon surface, which increases the density of the initial electrostatic charges. Finally, we assembled two free-standing samples to form a micrometre-thick stretchable self-powered sensor with the structure of Au–PDMS/Teflon/air gap/Teflon/PDMS–Au.

Fabrication of micrometre-thick implantable neural electrode

When we conducted the thermal evaporation process to make the ultrathin PDMS–Au conductor, we used a shadow mask to form patterned electrodes. After peeling off the ultrathin PDMS–Au conductor, we connected the patterned electrodes to a thin flexible circuit on polyimide (~ 15 μm) with a matched design via a 3M electrically conductive adhesive transfer tape 9703, further connected to a commercial flexible printed circuit that was compatible with the access port of the signal-recording equipment. Then, we treated the surfaces of the ultrathin PDMS–Au conductor and another ultrathin PDMS using an oxygen plasma treatment at a power of 30 W for 18 s, and we encapsulated parts of the ultrathin PDMS–Au conductor using the ultrathin PDMS by adhering them together with a gentle pressure of around 1 kPa. Due to the oxygen plasma treatment, such encapsulation was very strong without any detaching failure.

Next, we electroplated PEDOT/CNTs onto the exposed area of the ultrathin PDMS–Au conductor as the sensing electrodes, simultaneously performed on all the electrodes using an electrochemical workstation (CHI660D) with a conventional three-electrode configuration (platinum electrode as the counter electrode and Ag/AgCl as the reference electrode). To prepare the solution for electrodeposition, CNTs (Carbon Solutions, P3-SWNT) were suspended in deionized water at a concentration of 0.2 mg ml^{-1} by sonication, after which 3,4-ethylenedioxythiophene (Sigma-Aldrich) was added at a concentration of 0.01 M. Finally the deposition was conducted in a potentiostatic mode at 1.05 V for 15 min, and the electrode was soaked in deionized water for 1 min as the cleaning process.

Reporting summary

Further information on research design is available in the Nature Portfolio Reporting Summary linked to this article.

Data availability

The data that support the findings of this study are available from the corresponding authors on reasonable request.

Code availability

The codes used for analysing the neural signals are available from the corresponding authors upon reasonable request.

References

1. Kim, D. H. et al. Dissolvable films of silk fibroin for ultrathin conformal bio-integrated electronics. *Nat. Mater.* **9**, 511–517 (2010).
2. Liu, J. et al. Syringe-injectable electronics. *Nat. Nanotechnol.* **10**, 629–636 (2015).
3. Lee, S. et al. Nanomesh pressure sensor for monitoring finger manipulation without sensory interference. *Science* **370**, 966–970 (2020).
4. Liu, Y. et al. Morphing electronics enable neuromodulation in growing tissue. *Nat. Biotechnol.* **38**, 1031–1036 (2020).
5. Jeong, J. W. et al. Materials and optimized designs for human-machine interfaces via epidermal electronics. *Adv. Mater.* **25**, 6839–6846 (2013).
6. Someya, T., Bao, Z. & Malliaras, G. G. The rise of plastic bioelectronics. *Nature* **540**, 379–385 (2016).
7. Gao, W., Ota, H., Kiriya, D., Takei, K. & Javey, A. Flexible electronics toward wearable sensing. *Acc. Chem. Res.* **52**, 523–533 (2019).
8. Kang, S. K., Koo, J., Lee, Y. K. & Rogers, J. A. Advanced materials and devices for bioresorbable electronics. *Acc. Chem. Res.* **51**, 988–998 (2018).
9. Matsuhisa, N. et al. High-transconductance stretchable transistors achieved by controlled gold microcrack morphology. *Adv. Electron. Mater.* **5**, 1900347 (2019).
10. Lee, G. H. et al. Stretchable anisotropic conductive film (S-ACF) for electrical interfacing in high-resolution stretchable circuits. *Sci. Adv.* **8**, eabm3622 (2022).
11. Jiang, Z. et al. Highly stretchable metallic nanowire networks reinforced by the underlying randomly distributed elastic polymer nanofibers via interfacial adhesion improvement. *Adv. Mater.* **31**, e1903446 (2019).
12. Matsuhisa, N. et al. Printable elastic conductors by in situ formation of silver nanoparticles from silver flakes. *Nat. Mater.* **16**, 834–840 (2017).
13. Kim, Y. et al. Stretchable nanoparticle conductors with self-organized conductive pathways. *Nature* **500**, 59–63 (2013).
14. Son, D. et al. An integrated self-healable electronic skin system fabricated via dynamic reconstruction of a nanostructured conducting network. *Nat. Nanotechnol.* **13**, 1057–1065 (2018).

15. Chen, Z. et al. Three-dimensional flexible and conductive interconnected graphene networks grown by chemical vapour deposition. *Nat. Mater.* **10**, 424–428 (2011).
16. Choi, S. et al. Highly conductive, stretchable and biocompatible Ag–Au core–sheath nanowire composite for wearable and implantable bioelectronics. *Nat. Nanotechnol.* **13**, 1048–1056 (2018).
17. Jung, D. et al. Highly conductive and elastic nanomembrane for skin electronics. *Science* **373**, 1022–1026 (2021).
18. Liu, S., Shah, D. S. & Kramer-Bottiglio, R. Highly stretchable multilayer electronic circuits using biphasic gallium-indium. *Nat. Mater.* **20**, 851–858 (2021).
19. Ma, Z. et al. Permeable superelastic liquid-metal fibre mat enables biocompatible and monolithic stretchable electronics. *Nat. Mater.* **20**, 859–868 (2021).
20. Wang, Y. et al. Robust, self-adhesive, reinforced polymeric nanofilms enabling gas-permeable dry electrodes for long-term application. *Proc. Natl Acad. Sci. USA* **118**, e2111904118 (2021).
21. Lacour, S. P. et al. Mechanisms of reversible stretchability of thin metal films on elastomeric substrate. *Appl. Phys. Lett.* **88**, 204103 (2006).
22. Zhang, B. et al. Stretchable conductive fibers based on a cracking control strategy for wearable electronics. *Adv. Funct. Mater.* **28**, 1801683 (2018).
23. Liu, Z. et al. Highly stable and stretchable conductive films through thermal-radiation-assisted metal encapsulation. *Adv. Mater.* **31**, e1901360 (2019).
24. Johnston, I. D., McCluskey, D. K., Tan, C. K. L. & Tracey, M. C. Mechanical characterization of bulk Sylgard 184 for microfluidics and microengineering. *J. Micromech. Microeng.* **24**, 035017 (2014).
25. Liu, M., Sun, J. & Chen, Q. Influences of heating temperature on mechanical properties of polydimethylsiloxane. *Sens. Actuator A Phys.* **151**, 42–45 (2009).
26. Hadgraft, J. & Lane, M. E. Transepidermal water loss and skin site: a hypothesis. *Int. J. Pharm.* **373**, 1–3 (2009).
27. Geerligs, M. A literature review of the mechanical behavior of the stratum corneum, the living epidermis and the subcutaneous fat tissue (Philips Research, 2006).
28. Lee, H. et al. Stretchable organic optoelectronic devices: design of materials, structures, and applications. *Mater. Sci. Eng.* **146**, 100631 (2021).
29. Miyamoto, A. et al. Inflammation-free, gas-permeable, lightweight, stretchable on-skin electronics with nanomeshes. *Nat. Nanotechnol.* **12**, 907–913 (2017).
30. Yang, X. et al. Bioinspired neuron-like electronics. *Nat. Mater.* **18**, 510–517 (2019).
31. Mariello, M., Kim, K., Wu, K., Lacour, S. P. & Letierri, Y. Recent advances in encapsulation of flexible bioelectronic implants: materials, technologies and characterization methods. *Adv. Mater.* **34**, e2201129 (2022).
32. Zhang, Y. et al. Stretchable PDMS encapsulation via SiO₂ doping and atomic layer infiltration for flexible displays. *Adv. Mater. Interfaces* **9**, 2101857 (2022).
33. Ji, S. et al. Water-resistant conformal hybrid electrodes for aquatic enduring electrocardiographic monitoring. *Adv. Mater.* **32**, e2001496 (2020).
34. Jiang, Y. et al. Stretchable, washable, and ultrathin triboelectric nanogenerators as skin-like highly sensitive self-powered haptic sensors. *Adv. Funct. Mater.* **31**, 2005584 (2020).
35. Liu, Z. et al. Surface strain redistribution on structured microfibers to enhance sensitivity of fiber-shaped stretchable strain sensors. *Adv. Mater.* **30**, 1704229 (2018).
36. Mariello, M., Fachechi, L., Guido, F. & De Vittorio, M. Conformal, ultra-thin skin-contact-actuated hybrid piezo/triboelectric wearable sensor based on AlN and parylene-encapsulated elastomeric blend. *Adv. Funct. Mater.* **31**, 2101047 (2021).
37. Park, J., Kim, D. & Kim, Y. T. Ultra-stretchable on-body-based soft triboelectric nanogenerator for electronic skin. *Smart Mater. Struct.* **29**, 115031 (2020).
38. Chu, Y. et al. Human pulse diagnosis for medical assessments using a wearable piezoelectret sensing system. *Adv. Funct. Mater.* **28**, 1803413 (2018).
39. Cianchetti, M., Laschi, C., Menciassi, A. & Dario, P. Biomedical applications of soft robotics. *Nat. Rev. Mater.* **3**, 143–153 (2018).
40. Chen, N. et al. Nanotunnels within poly(3,4-ethylenedioxythiophene)-carbon nanotube composite for highly sensitive neural interfacing. *ACS Nano* **14**, 8059–8073 (2020).
41. Rijnbeek, E. H., Eleveld, N. & Olthuis, W. Update on peripheral nerve electrodes for closed-loop neuroprosthetics. *Front. Neurosci.* **12**, 350 (2018).
42. Musick, K. M. et al. Chronic multichannel neural recordings from soft regenerative microchannel electrodes during gait. *Sci. Rep.* **5**, 14363 (2015).
43. Alahi, M. E. E. et al. Recent advancement of electrocorticography (ECoG) electrodes for chronic neural recording/stimulation. *Mater. Today Commun.* **29**, 102853 (2021).

Acknowledgements

Parts of this work were conducted in RIKEN, Japan, supported by JSPS KAKENHI under grant nos. JP18H05469 and 17H06149. Parts of this work were conducted in Nanyang Technological University, Singapore, supported by the National Research Foundation Singapore (NRF) under NRF's Medium Sized Centre: Singapore Hybrid-Integrated Next-Generation μ -Electronics (SHINE) Centre funding programme and the Agency for Science, Technology and Research (A*STAR) under its AME Programmatic Funding Scheme (Project #A18A1b0045; X.C.). Parts of this work were conducted in the University of Macau, China, supported by the Science and Technology Development Fund, Macau SAR (FDCT) (file nos. 0059/2021/AFJ and 0040/2021/A1). The implantable experiments were conducted in the National University of Singapore and they were supported by the National Research Foundation, Prime Minister's Office, Singapore, under the NRF Investigatorship Programme (award no. NRF-NRFI05-2019-0003) and NUS NANONASH Programme (NUHSRO/2020/002/NanoNash/LOA; R143000B43114).

Author contributions

Z.J., K.F., X.C. and T.S. conceived and designed the research. Z.J. designed the the ultrathin PDMS–Au and performed the characterization of the mechanical, electrical and morphological properties. Z.J., S.J. and F.Z. designed the on-skin ECG sensor and performed the related characterizations. Z.J. and J.Z. designed the ultrathin sensor and performed the related characterizations. Z.J. and N.C. designed and fabricated the neural electrodes, and N.C. and Z.Y. performed the implantable experiments. R.L. and Yang Wang performed the COMSOL simulations. Yan Wang, H.L., Z.L., T.Y. and K.F. assisted in the experiment or analysed the data. All the authors discussed the results and commented on the manuscript. Z.J., K.F., X.L., X.C. and T.S. wrote the manuscript. We would like to thank Y. Jiang, J. Yi, W. Li and C. Cao from Nanyang Technological University and G. Gammad from National University of Singapore for their technical support and discussion.

Competing interests

The authors declare no competing interests.

Additional information

Supplementary information The online version contains supplementary material available at <https://doi.org/10.1038/s41928-022-00868-x>.

Correspondence and requests for materials should be addressed to Kenjiro Fukuda, Xiaodong Chen or Takao Someya.

Peer review information *Nature Electronics* thanks Xue Feng, Wei Gao, Massimo Mariello and the other, anonymous, reviewer(s) for their contribution to the peer review of this work.

Reprints and permissions information is available at www.nature.com/reprints.

Publisher's note Springer Nature remains neutral with regard to jurisdictional claims in published maps and institutional affiliations.

Springer Nature or its licensor (e.g. a society or other partner) holds exclusive rights to this article under a publishing agreement with the author(s) or other rightsholder(s); author self-archiving of the accepted manuscript version of this article is solely governed by the terms of such publishing agreement and applicable law.

© The Author(s), under exclusive licence to Springer Nature Limited 2022

Reporting Summary

Nature Research wishes to improve the reproducibility of the work that we publish. This form provides structure for consistency and transparency in reporting. For further information on Nature Research policies, see our [Editorial Policies](#) and the [Editorial Policy Checklist](#).

Statistics

For all statistical analyses, confirm that the following items are present in the figure legend, table legend, main text, or Methods section.

n/a Confirmed

- | | | |
|-------------------------------------|-------------------------------------|--|
| <input type="checkbox"/> | <input checked="" type="checkbox"/> | The exact sample size (n) for each experimental group/condition, given as a discrete number and unit of measurement |
| <input type="checkbox"/> | <input checked="" type="checkbox"/> | A statement on whether measurements were taken from distinct samples or whether the same sample was measured repeatedly |
| <input checked="" type="checkbox"/> | <input type="checkbox"/> | The statistical test(s) used AND whether they are one- or two-sided
<i>Only common tests should be described solely by name; describe more complex techniques in the Methods section.</i> |
| <input checked="" type="checkbox"/> | <input type="checkbox"/> | A description of all covariates tested |
| <input checked="" type="checkbox"/> | <input type="checkbox"/> | A description of any assumptions or corrections, such as tests of normality and adjustment for multiple comparisons |
| <input type="checkbox"/> | <input checked="" type="checkbox"/> | A full description of the statistical parameters including central tendency (e.g. means) or other basic estimates (e.g. regression coefficient) AND variation (e.g. standard deviation) or associated estimates of uncertainty (e.g. confidence intervals) |
| <input type="checkbox"/> | <input checked="" type="checkbox"/> | For null hypothesis testing, the test statistic (e.g. F , t , r) with confidence intervals, effect sizes, degrees of freedom and P value noted
<i>Give P values as exact values whenever suitable.</i> |
| <input checked="" type="checkbox"/> | <input type="checkbox"/> | For Bayesian analysis, information on the choice of priors and Markov chain Monte Carlo settings |
| <input checked="" type="checkbox"/> | <input type="checkbox"/> | For hierarchical and complex designs, identification of the appropriate level for tests and full reporting of outcomes |
| <input checked="" type="checkbox"/> | <input type="checkbox"/> | Estimates of effect sizes (e.g. Cohen's d , Pearson's r), indicating how they were calculated |

Our web collection on [statistics for biologists](#) contains articles on many of the points above.

Software and code

Policy information about [availability of computer code](#)

Data collection For this study the following software was used to collect data: BACAS for ECG signal recording, Labview 2020 for the mechanical sensor, Intan RHX for CMAP and CNAP signal recording

Data analysis Matlab 2021b, Excel, Origin 2018

For manuscripts utilizing custom algorithms or software that are central to the research but not yet described in published literature, software must be made available to editors and reviewers. We strongly encourage code deposition in a community repository (e.g. GitHub). See the Nature Research [guidelines for submitting code & software](#) for further information.

Data

Policy information about [availability of data](#)

All manuscripts must include a [data availability statement](#). This statement should provide the following information, where applicable:

- Accession codes, unique identifiers, or web links for publicly available datasets
- A list of figures that have associated raw data
- A description of any restrictions on data availability

The data and custom codes that support the findings and plots of this study are available from the corresponding authors upon reasonable request

Field-specific reporting

Please select the one below that is the best fit for your research. If you are not sure, read the appropriate sections before making your selection.

Life sciences Behavioural & social sciences Ecological, evolutionary & environmental sciences

For a reference copy of the document with all sections, see [nature.com/documents/nr-reporting-summary-flat.pdf](https://www.nature.com/documents/nr-reporting-summary-flat.pdf)

Life sciences study design

All studies must disclose on these points even when the disclosure is negative.

Sample size	6 samples were used for on-skin ECG sensors and 5 samples were used for the mechanical sensors; 4 adult male Sprague-Dawley rats were used for the implantable experiments, where both the ultrathin electrodes and control devices were tested.
Data exclusions	No data was excluded from the analysis.
Replication	All electronic devices were successfully prepared by the same fabrication procedures described in the manuscript, and they were repeated at least three times independently for each group with similar results.
Randomization	Subjects were randomly assigned to experimental groups
Blinding	Blinding was not relevant to our experiment as there were no subjective elements to assessing the device's capabilities.

Reporting for specific materials, systems and methods

We require information from authors about some types of materials, experimental systems and methods used in many studies. Here, indicate whether each material, system or method listed is relevant to your study. If you are not sure if a list item applies to your research, read the appropriate section before selecting a response.

Materials & experimental systems

n/a	Involvement in the study
<input checked="" type="checkbox"/>	<input type="checkbox"/> Antibodies
<input checked="" type="checkbox"/>	<input type="checkbox"/> Eukaryotic cell lines
<input checked="" type="checkbox"/>	<input type="checkbox"/> Palaeontology and archaeology
<input type="checkbox"/>	<input checked="" type="checkbox"/> Animals and other organisms
<input type="checkbox"/>	<input checked="" type="checkbox"/> Human research participants
<input checked="" type="checkbox"/>	<input type="checkbox"/> Clinical data
<input checked="" type="checkbox"/>	<input type="checkbox"/> Dual use research of concern

Methods

n/a	Involvement in the study
<input checked="" type="checkbox"/>	<input type="checkbox"/> ChIP-seq
<input checked="" type="checkbox"/>	<input type="checkbox"/> Flow cytometry
<input checked="" type="checkbox"/>	<input type="checkbox"/> MRI-based neuroimaging

Animals and other organisms

Policy information about [studies involving animals](#); [ARRIVE guidelines](#) recommended for reporting animal research

Laboratory animals	The experiments were performed in four adult male Sprague–Dawley rats (350–600 g). Animal care and related procedures were approved by the IACUC of National University of Singapore.
Wild animals	No wild animals were used in the study
Field-collected samples	No field collected samples were used in the study
Ethics oversight	The study protocol related to the implantable experiment was thoroughly reviewed and approved by the IACUC of National University of Singapore (Protocol No. R20-1312).

Note that full information on the approval of the study protocol must also be provided in the manuscript.

Human research participants

Policy information about [studies involving human research participants](#)

Population characteristics	Age: 26-35 years old. Male healthy subjects
Recruitment	Subject were recruited from RIKEN and Nanyang Technological University. The subjects were voluntary. There is no potential self-selection bias.

Ethics oversight

The study protocol related to on-skin ECG sensors was thoroughly reviewed and approved by the ethical committee of Nanyang Technological University (Approval No. IRB-2017-08-035-01). The study protocol related to the mechanical sensors was thoroughly reviewed and approved by the ethical committee of RIKEN (Approval No. Wako3 30-32).

Note that full information on the approval of the study protocol must also be provided in the manuscript.